

Article

# Numerical Investigation for Nonlinear Thermal Radiation in MHD Cu–Water Nanofluid Flow in a Channel with Convective Boundary Conditions

Tunde Abdulkadir Yusuf <sup>1,\*</sup>, Adeshina Taofeeq Adeosun <sup>2</sup>, Victor Olajide Akinsola <sup>1</sup>,  
Ramoshweu Solomon Lebelo <sup>3</sup> and Oluwadamilare Joseph Akinremi <sup>4</sup>

<sup>1</sup> Department of Mathematics, Adeleke University, Ede 232104, Nigeria; akinsolaolajide@adelekeuniversity.edu.ng

<sup>2</sup> Department of Mathematics, Federal College of Education, Iwo 232102, Nigeria; adeshinata@fceiwo.edu.ng

<sup>3</sup> Education Department, Vaal University of Technology, Vanderbijlpark 1911, South Africa; sollyl@vut.ac.za

<sup>4</sup> Department of Mathematics, Landmark University, Omu-Aran 251103, Nigeria; akinremi.joseph@lmu.edu.ng

\* Correspondence: tunde.yusuf@adelekeuniversity.edu.ng

**Abstract:** The implications of nonlinear thermal radiation on a Cu–water nanofluid flow with varying viscosity characteristics and convective boundary conditions are investigated numerically in this article. The nonlinear model takes the combined effects of Joule dissipation and Ohmic heating into consideration. The Spectral Local Linearization Method (SLLM) is used to address the nonlinear governing model. The numerical investigation’s findings were conducted and compared with the existing study. In Cu–water nanofluid flows with variable viscosity and convective boundary conditions, nonlinear thermal radiation plays an important role, as this work insightfully demonstrates. Pertinent results for velocity, temperature, skin friction, and heat transfer rate are displayed graphically and discussed quantitatively with respect to various parameters embedded in the model. The results revealed that the Cu–water thermal distribution lessens as the nanoparticle volume fraction upsurges. The outcomes of this study have potential applications in industrial systems such as power plants, cooling systems, and climate control systems.

**Keywords:** water-copper nanoparticles; permeable channel; variable viscosity; nonlinear radiative heat flux; convective boundary conditions; numerical method

**MSC:** 37N10



**Citation:** Yusuf, T.A.; Adeosun, A.T.; Akinsola, V.O.; Lebelo, R.S.; Akinremi, O.J. Numerical Investigation for Nonlinear Thermal Radiation in MHD Cu–Water Nanofluid Flow in a Channel with Convective Boundary Conditions. *Mathematics* **2023**, *11*, 3409. <https://doi.org/10.3390/math11153409>

Academic Editor: Marco Pedroni

Received: 16 June 2023

Revised: 13 July 2023

Accepted: 3 August 2023

Published: 4 August 2023



**Copyright:** © 2023 by the authors. Licensee MDPI, Basel, Switzerland. This article is an open access article distributed under the terms and conditions of the Creative Commons Attribution (CC BY) license (<https://creativecommons.org/licenses/by/4.0/>).

## 1. Introduction

Fluids incorporating solid-sized nanoparticles are referred to as “nanofluids”. Natural or induced convection in enclosures has been a very active field of research over the last few decades. Nanofluids exhibit exceptional qualities such as high thermal conductivity, little clogging in flow passageways, long-term stability, and homogeneity due to the nanoparticles’ tiny sizes and extremely large specific surface areas [1]. In the thermal sector, nanoparticles are utilized to boost transformer coolant efficiency and enhance heat transmission from solar collectors to storage tanks. In addition to improving the transfer of heat, the use of nanofluids in thermal management systems also results in smaller and lighter heat exchangers. The contemporary trend in nano liquid in view of their application is observed by Giwa et al. [2]. Younes et al. [3] investigated the thermal efficiency impact on nanofluid and their application. Recently, the interaction between heat transport and magnetohydrodynamic nanofluid was studied by Gürdal et al. [4]. In order to potentially save solar energy, Hussain et al. [5] looked at the heat characteristics of Maxwell nanofluids movements of a solar concentrator. In a microchannel with a porous regime, Wang et al. [6] simulation of nanofluid flow was conducted. In the more expansive

framework of magnetohydrodynamics (MHD), some basic flow issues related to classical hydrodynamics have attracted attention recently. The heat emission characteristics of a hydromagnetic effect of nanofluid flow through a spinning system were explored by Satya Narayana et al. [7]. Izadi et al. [8] emphasize the MHD thermal gravitational circulation of a spinning nanofluid in a permeable container.

Fluid viscosity is a crucial component of the nanofluid heat transfer process. In virtually all situations, the coefficient of viscosity for real fluids is said to be temperature and pressure dependent. For liquids (say, water and oils), the highest prevailing effect of viscosity variation is accounted for by temperature. For various thermal system processes, it is established that heat distribution within the flow channel is non-uniform; hence fluid viscosity sometimes visibly changes with a large temperature difference [9]. In most of the studies of this type of problem, the viscosity of the fluid is assumed to be constant. To better understand the viscosity variation characteristic of nanofluids, a variety of studies have been carried out. Nasrin and Alim [1] used a water/Cu nanofluid and variations in the viscosity of aided convective flow via a riser pipe of a horizontal flat plate solar collector to quantitatively assess thermal efficiency. The findings demonstrate that altering the values of viscosity may offer heat transfer via the more efficient collector. A helpful tool for describing and predicting the temperature dependence of fluid flow, the Arrhenius form of variable viscosity allows for a greater understanding of a variety of natural and industrial processes. Molaledi and Makinde [9] examined the Couette flow of water-based copper nanofluid with variable viscosity features of the Arrhenius form. The variable viscosity property effect of the motion of a water-based nanofluid utilizing nanoparticles separated by two spinning disks was explored by Bhandari et al. [10]. Recently, Adesanya et al. [11] presented the magnetized couple stress fluid flow over a slanted Riga surface with variable viscosity.

In the fields of thermal sciences and nanotechnology, the study of nanoparticles in a base fluid in the presence of heat radiation has captured the attention of scientists and researchers in significant ways. The behaviour of a Cu nanoparticle in a water-based nanofluid with the influence of heat radiation was examined by Kumar et al. [12]. They observed that the Nusselt number improved as heat radiation and Rayleigh number rose, but the number of Hartmann grew in the opposite direction. The consequences of thermal emission on the heat transfer variation in Casson fluid flow across an undulating surface were discussed by Khan et al. [13]. Al-Mdallal et al. [14] looked at the thermal characteristics of a water-based Cu nanofluid when radiation was present. The temperature and radiative heat transfer are frequently assumed to have a linear connection in conventional heat transfer estimations, but in certain cases, nonlinear effects become significant, especially at high temperatures or when considering nanoscale phenomena. Nonlinear thermal radiation describes the transfer of heat energy through radiation, which follows a nonlinear relationship with temperature. A radially extended disk was employed as a medium by Khan et al. [15] to assess the influence of entropy generation imposed by nonlinear thermal radiation on the Carreau nanofluid. Rooman et al. [16] looked at the dissipation effect as well as the nonlinear radiative flux in nanofluid flow induced by a stretching cylinder. Their findings show that the heat transfer rate is a decreasing effect of the temperature ratio.

Much less effort has been devoted to examining nanofluid flow problems of temperature-dependent viscosity and the combined effects of nonlinear thermal radiation, imposed magnetic field and convective heat exchange at the channel surface. The main objective of this present study is to bridge this information gap. Moreover, water is viewed as a universal solvent that is affordable and simple to use. Water-based nanofluids are extensively used in many industrial processes as heat exchangers. Due to its high pH and low surface tension, which allow for the free movement of nanoparticles on its surface, it is suggested as the being most functional base fluid. The copper nanoparticle is appealing for a variety of applications due to its distinctive mix of thermal, optical, and antibacterial properties. As a result, the main aim of this current work is to numerically examine the effect of varying Cu–water nanofluid viscosity in the context of radiative effect-influenced heat

transfer across a permeable channel. The impacts of captured thermophysical parameters are presented in graphs and discussed quantitatively.

### 2. Mathematical Model

Consider a channel with walls assumed to be electrically non-conducting that is filled with an optically dense radiating nanofluid that also assumes the conditions of incompressible, laminar, electrically conducting, fully developed forced convection. As displayed in Figure 1, the flow of the water-based nanofluid, which is thought of as a single-phase flow, occurs in the  $x$  direction between two parallel leaky plates with walls spaced  $h$  distances apart. Both the lower plate and the top plate are held motionless. A steady magnetic field  $B$  is provided in the direction of the  $y$ -axis to the flow. The nanoparticle is considered a single-phase flow and is assumed to be in thermal equilibrium with water. It is also assumed that there is no slip flow between the nanoparticles and water. In addition, the nanoparticle heat transfer analysis is maintained by considering temperatures  $T_1$  and  $T_2$  lower and upper walls of the channel. Thermal radiation and dissipation are also put into account.

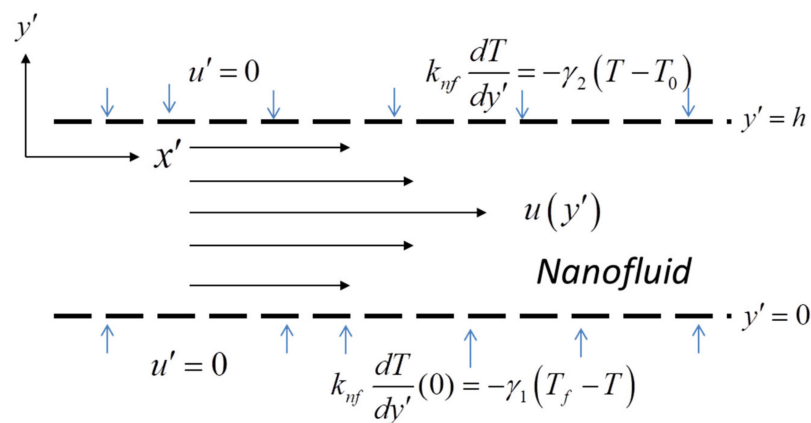


Figure 1. Flow Geometry.

Under these aforementioned conditions, the model mathematical formulation of momentum and energy equation may be written as Molaledi and Makinde [9]

$$\rho_{nf} v_0 \frac{du'}{dy'} = -\frac{dp'}{dx'} + \frac{d}{dy'} \left( \mu_{nf} \frac{du'}{dy'} \right) - \sigma_{nf} B_0 u', \tag{1}$$

$$(\rho c_p)_{nf} v_0 \frac{dT}{dy'} = k_{nf} \frac{d^2 T}{dy'^2} - \frac{dq_r}{dy'} + \mu_{nf} \left( \frac{du'}{dy'} \right)^2 + \sigma_{nf} B_0 u'^2 \tag{2}$$

and the boundary constraints

$$u'(0) = 0, \quad k_{nf} \frac{dT}{dy'}(0) = -\gamma_1 (T_f - T(0)), \tag{3}$$

$$u'(h) = 0, \quad k_{nf} \frac{dT}{dy'}(h) = -\gamma_2 (T(h) - T_0) \tag{4}$$

where  $u'$  is the velocity component in the  $x$  direction,  $v_0$  is the suction/injection velocity at the channel walls,  $\rho_{nf}$  is the nanofluid density,  $k_{nf}$  is the nanofluid thermal conductivity,  $T$  is the nanofluid temperature,  $\sigma_{nf}$  is the nanofluid electrical conductivity,  $B_0$  is the magnetic field imposed along the  $y'$ -axis, and  $(\rho C_p)_{nf}$  is the nanofluid heat capacitance. Moreso,  $\gamma_1$  and  $\gamma_2$  are the heat transfer coefficients at the lower and upper walls, respectively,  $T_0$  is the fluid initial temperature,  $T_f$  is the ambient temperature. Following [9], the nanofluid temperature-dependent viscosity ( $\mu_{nf}$ ) is described in Arrhenius form as

$$\mu_{nf} = \frac{\mu_f e^{\frac{E}{RT}}}{(1 - \phi)^{2.5}}, \tag{5}$$

and the Rosseland approximation is expressed nonlinearly in the form

$$q_r = -\frac{4\sigma^*}{3k^*} \frac{\partial T^4}{\partial y'} = -\frac{16\sigma^*}{3k^*} T^3 \frac{\partial T}{\partial y'}, \tag{6}$$

where  $\sigma^*$  is the Stefan Boltzmann constant and  $k^*$  is the mean observation constant. Further, the thermophysical expressions of nanofluid are given below and also in Table 1 as:

$$\frac{\sigma_{nf}}{\sigma_f} = 1 + \left[ \frac{3(\frac{\sigma_s}{\sigma_f} - 1)\phi}{(\frac{\sigma_s}{\sigma_f} + 2) - (\frac{\sigma_s}{\sigma_f} - 1)\phi} \right], \quad \frac{\rho_{nf}}{\rho_f} = (1 - \phi) + \phi \frac{\rho_s}{\rho_f},$$

$$\frac{(\rho c_p)_{nf}}{(\rho c_p)_f} = (1 - \phi) + \phi \frac{(\rho c_p)_s}{(\rho c_p)_f}, \quad \frac{k_{nf}}{k} = \frac{k_s + (m-1)k_f - (m-1)\phi(k_f - k_s)}{k_s + (m-1)k_f + \phi(k_f - k_s)}.$$

**Table 1.** Thermo-physical properties of fluid and nanoparticles.

	$\rho$ (kg/m <sup>3</sup> )	$C_p$ (J/kgK)	$k$ (W/mK)	$\sigma$ (Sm)
Fluid phase (Water)	997.1	4179	0.613	0.05
Cu	8933	385	400	$5.96 \times 10^7$

Introducing the dimensionless parameters

$$u = \frac{u'}{v_0}, \quad y = \frac{y'}{h}, \quad x = \frac{x'}{h}, \quad \theta = \frac{E(T - T_0)}{RT_0^2}. \tag{7}$$

After the use of Equation (7) on Equations (1) and (2), the dimensionless form is

$$AR \frac{du}{dy} = G + \frac{e^{\frac{1}{\gamma}} e^{-\frac{\theta}{1+\gamma\theta}}}{(1 - \phi)^{2.5}} \left( \frac{d^2u}{dy^2} - \frac{1}{(1 + \gamma\theta)^2} \frac{d\theta}{dy} \frac{du}{dy} \right) - DMu, \tag{8}$$

$$CRPr \frac{d\theta}{dy} = B \frac{d^2\theta}{dy^2} + \frac{d}{dy} \left( Rd(\gamma\theta + 1)^3 \frac{d\theta}{dy} \right) + \frac{e^{\frac{1}{\gamma}} e^{-\frac{\theta}{1+\gamma\theta}}}{(1 - \phi)^{2.5}} EcPr \left( \frac{du}{dy} \right)^2 + DEcPrMu^2, \tag{9}$$

and the boundary conditions (3) and (4):

$$\frac{d\theta}{dy}(0) = \frac{\beta_1}{B}(\theta(0) - 1), \quad u(0) = 0, \quad \frac{d\theta}{dy}(1) = -\frac{\beta_2}{B}\theta(1), \quad u(1) = 0 \tag{10}$$

where

$$G = -\frac{dp}{dx}, \quad R = \frac{v_0 h \rho_f}{\mu_f}, \quad Pr = \frac{\mu_f c_{pf}}{k_f}, \quad Ec = \frac{v_0^2 E}{c_{pf} RT_0^2}, \quad Rd = \frac{16\sigma^* T_0^3}{3k^* k_f}, \quad M = \frac{\sigma_f h^2 B_0^2}{\mu_f},$$

$$p = \frac{h \hat{p}}{\mu_f v_0}, \quad \gamma = \frac{RT_0}{E}, \quad \beta_1 = \frac{\gamma_1 h}{k_f}, \quad \beta_2 = \frac{\gamma_2 h}{k_f}, \quad B = \frac{k_s + (m-1)k_f - (m-1)\phi(k_f - k_s)}{k_s + (m-1)k_f + \phi(k_f - k_s)}, \tag{11}$$

$$A = (1 - \phi) + \phi \frac{\rho_s}{\rho_f}, \quad C = (1 - \phi) + \phi \frac{(\rho c_p)_s}{(\rho c_p)_f}, \quad D = 1 + \left[ \frac{3\left(\frac{\sigma_s}{\sigma_f} - 1\right)\phi}{\left(\frac{\sigma_s}{\sigma_f} + 2\right) - \left(\frac{\sigma_s}{\sigma_f} - 1\right)\phi} \right].$$

In (11),  $G$  denotes the pressure gradient parameter,  $R$  is Reynolds number,  $Pr$  is the Prandtl number. The Eckert number and radiation parameter are denoted by  $Ec$  and  $Rd$ , respectively.  $M$  denotes the magnetic field;  $\gamma$  is the activation energy parameter while  $\beta_1$  and  $\beta_2$  are the Biot numbers for the lower and upper wall, respectively.

*Skin Friction and Nusselt Number*

The formulas for skin friction coefficients are:

$$C_f = \frac{\tau_w}{\rho_f U^2} = \frac{e^{\frac{1}{\gamma}} e^{-(\frac{\theta}{1+\gamma\theta})}}{R(1-\phi)^{2.5}} \frac{du}{dy} \Big|_{y=1}, \quad Nu = \frac{q_w}{k_f R T_w^2} = -\left(B + Rd(\gamma\theta + 1)\right)^3 \frac{d\theta}{dy} \Big|_{y=1}, \quad (12)$$

which define surface shear stress  $\tau_w$  and the wall heat flux  $q_w$  as:

$$\tau_w = \mu_{nf} \frac{\partial u'}{\partial y'}, \quad q_w = -k_{nf} \left(1 + \frac{16\sigma^* T^3}{3k^* k_f}\right) \frac{\partial T}{\partial y'}$$

**3. Method of Solution**

The Spectral Local Linearization Method (SLLM) is used to address the boundary value problem (8)–(10). Details on this method can be found in [17–22]. To implement SLLM, governing Equations (8) and (9) are, respectively, denoted by  $U$  and  $\Theta$ , as follows:

$$U = G + \frac{e^{\frac{1}{\gamma}} e^{-(\frac{\theta}{1+\gamma\theta})}}{(1-\phi)^{2.5}} \left( \frac{d^2 u}{dy^2} - \frac{1}{(1+\gamma\theta)^2} \frac{d\theta}{dy} \frac{du}{dy} \right) - DMu - AR \frac{du}{dy}, \quad (13)$$

$$\Theta = B \frac{d^2 \theta}{dy^2} + \frac{d}{dy} \left( Ra(\gamma\theta + 1)^3 \frac{d\theta}{dy} \right) + \frac{e^{\frac{1}{\gamma}} e^{-(\frac{\theta}{1+\gamma\theta})}}{(1-\phi)^{2.5}} EcPr \left( \frac{du}{dy} \right)^2 + DEcPrMu^2 - CRePr \frac{d\theta}{dy}. \quad (14)$$

Equations (13) and (14) are first linearized locally by adopting quazilinearization method to obtain

$$\begin{aligned} a_{0r} \frac{d^2 u_{r+1}}{dy^2} + a_{1r} \frac{du_{r+1}}{dy} + a_{2r} u_{r+1} &= R_{1,r}, \\ b_{0r} \frac{d^2 \theta_{r+1}}{dy^2} + b_{1r} \frac{d\theta_{r+1}}{dy} + b_{2r} \theta_{r+1} &= R_{2,r}, \end{aligned} \quad (15)$$

with the corresponding boundary conditions

$$\begin{aligned} u_{r+1}(0) &= 0, \quad \frac{d\theta_{r+1}}{dy}(0) - \frac{Bi_1}{B} \theta_{r+1}(0) = -\frac{Bi_1}{B} \theta_f, \\ u_{r+1}(1) &= 0, \quad \frac{d\theta_{r+1}}{dy}(1) + \frac{Bi_2}{B} \theta_{r+1}(1) = 0, \end{aligned} \quad (16)$$

where

$$\left. \begin{aligned} a_{0r} &= \frac{\partial U}{\partial \left( \frac{d^2 u}{dy^2} \right)} = \frac{e^{\left(\frac{1}{\gamma}\right)} e^{-\left(\frac{\theta_r}{\gamma\theta_r+1}\right)}}{(1-\phi)^{2.5}}, \quad a_{1r} = \frac{\partial U}{\partial \left( \frac{du}{dy} \right)} = -\frac{\frac{d\theta_r}{dy} e^{\left(\frac{1}{\gamma}\right)} e^{-\left(\frac{\theta_r}{\gamma\theta_r+1}\right)}}{(1-\phi)^{2.5} (\gamma\theta_r+1)^2} - AR, \quad a_{2r} = \frac{\partial U}{\partial (u)} = -DM \\ b_{0r} &= \frac{\partial \Theta}{\partial \left( \frac{d^2 \theta}{dy^2} \right)} = B + Ra(\gamma\theta_r+1)^3, \quad b_{1r} = \frac{\partial \Theta}{\partial \left( \frac{d\theta}{dy} \right)} = 6\gamma \frac{d\theta_r}{dy} Ra(\gamma\theta_r+1)^2 - CPrR, \\ b_{2r} &= \frac{\partial \Theta}{\partial (\theta)} = -\frac{Ec \left( \frac{du_r}{dy} \right)^2 Pre^{\left(\frac{1}{\gamma}\right)} e^{-\left(\frac{\theta_r}{\gamma\theta_r+1}\right)}}{(1-\phi)^{2.5} (\gamma\theta_r+1)^2} + 6\gamma^2 \left( \frac{d\theta_r}{dy} \right)^2 Ra(\gamma\theta_r+1) + 3\gamma \frac{d^2 \theta_r}{dy^2} Ra(\gamma\theta_r+1)^2 \\ R_{1,r} &= a_{0r} \frac{d^2 u_r}{dy^2} + a_{1r} \frac{du_r}{dy} + a_{2r} u_r - U_r, \quad R_{2,r} = b_{0r} \frac{d^2 \theta_r}{dy^2} + b_{1r} \frac{d\theta_r}{dy} + b_{2r} \theta_r - \Theta_r \end{aligned} \right\}. \quad (17)$$

The initial approximations  $u_r$  and  $\theta_r$  required to start the iteration (15) are chosen to be functions satisfied the boundary conditions. Thus, the suitable initial approximations are given as

$$u_r = 0, \quad \theta_r = \frac{\beta_1 \theta_f (B + \beta_2) - \beta_1 \beta_2 \theta_f y}{B\beta_1 + B\beta_2 + \beta_1 \beta_2}. \quad (18)$$

The next step is to use the spectral collocation method repeatedly to solve the resulting linear Equation (15) with boundary conditions (16). For the sake of conciseness, the spectral collocation approach is not covered in depth in this study. It is appropriate to transfer the domain on which the governing equation is defined to the interval where the spectral

technique may be used before using the spectral approach. To map the interval  $[0, 1]$  to  $[-1, 1]$ , we utilize the transformation  $y = \frac{x+1}{2}$ . The fundamental idea of the spectral collocation method is that of a differentiation matrix  $D$  which is employed to approximate the derivative of the unknown variables  $u(y)$  and  $\theta(y)$  at the collocation points of the matrix–vector product.

$\frac{du(y)}{dy} = \sum_{k=0}^N \mathbf{D}_{i,k}u(x_k) = \mathbf{D}\mathbf{u}$  and  $\frac{d\theta(y)}{dy} = \sum_{k=0}^N \mathbf{D}_{i,k}\theta(x_k) = \mathbf{D}\theta$ , where  $N$  is the number of collocation points,  $\mathbf{D} = 2D$ ,  $\mathbf{u} = [u(x_0), u(x_1), \dots, u(x_N)]^T$ , and  $\theta = [\theta(x_0), \theta(x_1), \dots, \theta(x_N)]^T$  are the vector functions at the collocation points. Higher order derivatives are obtained as powers of  $\mathbf{D}$ , that is

$\frac{d^n u(y)}{dy^n} = \sum_{k=0}^N \mathbf{D}^n_{i,k}u(x_k) = \mathbf{D}^n\mathbf{u}$  and  $\frac{d^n \theta(y)}{dy^n} = \sum_{k=0}^N \mathbf{D}^n_{i,k}\theta(x_k) = \mathbf{D}^n\theta$ , where  $n$  is the order of the derivative.

Applying the spectral collocation method with derivative matrices on Equations (15) and (16) yield

$$\begin{aligned} \mathbf{A}_1\mathbf{u}_{r+1} &= \mathbf{R}_{1,r}, \\ \mathbf{A}_2\theta_{r+1} &= \mathbf{R}_{2,r}, \end{aligned} \tag{19}$$

with corresponding boundary conditions

$$\begin{aligned} u_{r+1}(x_N) &= 0, \sum_{k=0}^N \mathbf{D}_{N,k}\theta_{r+1}(x_k) - \frac{Bi_1}{B}\theta_{r+1}(x_N) = -\frac{Bi_1}{B}\theta_f, \\ u_{r+1}(x_0) &= 0, \sum_{k=0}^N \mathbf{D}_{0,k}\theta_{r+1}(x_k) + \frac{Bi_2}{B}\theta_{r+1}(x_0) = 0, \end{aligned} \tag{20}$$

here

$$\begin{aligned} \mathbf{A}_1 &= \text{diag}(a_{0r})\mathbf{D}^2 + \text{diag}(a_{1r})\mathbf{D} + \text{diag}(a_{2r})\mathbf{I}, \\ \mathbf{A}_2 &= \text{diag}(b_{0r})\mathbf{D}^2 + \text{diag}(b_{1r})\mathbf{D} + \text{diag}(b_{2r})\mathbf{I} \\ \mathbf{R}_{1,r} &= a_{0r}\mathbf{D}^2\mathbf{u}_r + a_{1r}\mathbf{D}\mathbf{u}_r + a_{2r}\mathbf{u}_r - \mathbf{U}_r, \\ \mathbf{R}_{2,r} &= b_{0r}\mathbf{D}^2\theta_r + b_{1r}\mathbf{D}\theta_r + b_{2r}\theta_r - \Theta_r. \end{aligned} \tag{21}$$

Equations (19) and (20) are solved iteratively until the desired solution is obtained.

*Analysis of Numerical Convergence, Error and Stability of the Method*

The method’s convergence and stability are assessed by taking into account the norm of the difference in the values of the functions between two subsequent iterations as

$$E_u = \text{Max}\|u_{r+1} - u_r\|, E_\theta = \text{Max}\|\theta_{r+1} - \theta_r\| \tag{22}$$

$E_u$  and  $E_\theta$  decrease swiftly as the number of iterations increases (see Figure 2). This shows that LLM converges within a few iterations. Furthermore, a convergence of the numerical scheme for Skin friction and Nuselt number as a function of collocation points is computed in Table 2.

**Table 2.** Convergence of Skin friction and Nuselt number for different collocation points when:  $\beta_1 = 1, \beta_2 = 1, \theta_f = 1, \phi = 0.01, M = 1, Ra = 0.5, \gamma = 1, Pr = 6.8, Ec = 0.1, G = 1, R = 1, m = 3, r = 20$ .

Collocation Points (N)	$C_f$	$Nu$
5	0.4247578180	0.3774410096
10	0.4246332084	0.3732542791
15	0.4246333494	0.3732579467
20	0.4246333493	0.3732579407
25	0.4246333493	0.3732579407
30	0.4246333493	0.3732579407

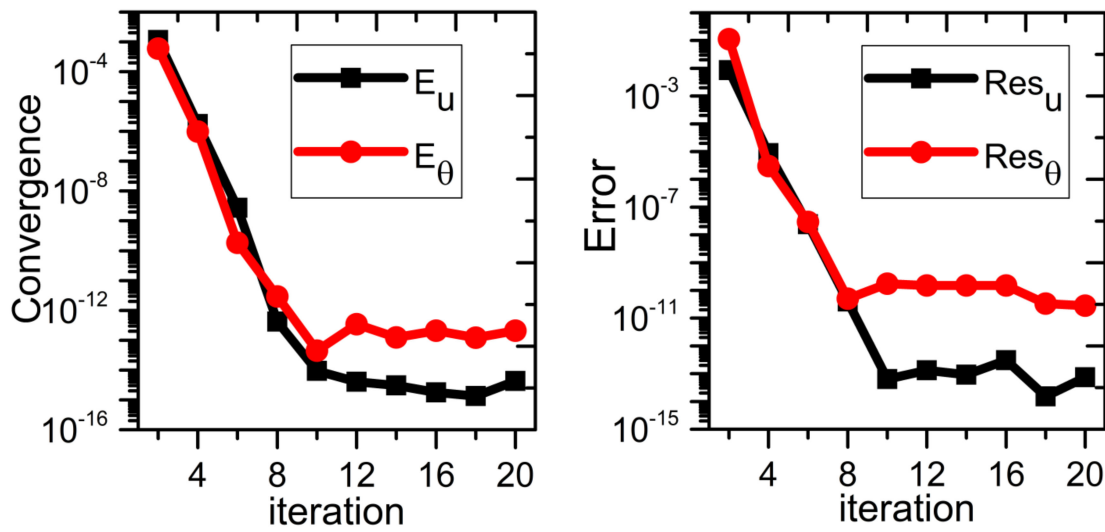


Figure 2. Residual Error.

Also, residual error norms are computed to show the accuracy of LLM. Residual error norms are given as

$$R_u = \text{Max} \|U(u, \theta)\|, R_\theta = \text{Max} \|\Theta(u, \theta)\| \tag{23}$$

where  $U(u, \theta)$  and  $\Theta(u, \theta)$  are nonlinear differential Equations (13) and (14), respectively. Residual errors are found to decrease rapidly with an increasing number of iterations, as depicted in Figure 2. However, the residual error  $\Theta(u, \theta)$  is not as minimum as  $U(u, \theta)$  because the energy equation is strongly nonlinear compared to the momentum equation. Table 3 shows the validation of velocity profile results with the work of Makinde and Egunjobi [23], which elucidates that the values obtained from the solution techniques agree well with those results obtained by Makinde and Egunjobi [23]. Furthermore, in Tables 4 and 5, the validation of velocity and temperature profile solutions with the ones obtained via the regular fourth-order Runge-Kutta method (RK4) is presented. RK4 is executed by utilising the NDSolve command in Wolfram *Mathematica*. As shown in both tables, a good agreement between the solutions is recorded, and both solutions match each other with an average absolute error of  $10^{-9}$ .

Table 3. Validation of LLM results for velocity when:  $\phi = 0, \gamma = \infty, G = 1, R = 1$ .

$y$	$u_{LLM}(y)$	Makinde and Egunjobi [23]	$ u_{LLM} - u_{RK4} $
0.0	0.0000000000	0.00000000	0.00000000
0.1	0.0387929829	0.03879297	$1.29401 \times 10^{-8}$
0.2	0.0711487741	0.071148750	$2.40614 \times 10^{-8}$
0.3	0.0963903478	0.09639032	$2.78057 \times 10^{-8}$
0.4	0.1137695200	0.11376948	$4.00103 \times 10^{-8}$
0.5	0.1224593312	0.12245933	$1.18527 \times 10^{-8}$
0.6	0.1215460526	0.12154600	$5.25610 \times 10^{-8}$
0.7	0.1100195730	0.11001953	$4.30211 \times 10^{-8}$
0.8	0.0867637675	0.08676372	$4.74739 \times 10^{-8}$
0.9	0.0505450044	0.05054498	$2.43530 \times 10^{-8}$
1.0	0.0000000000	0.00000000	0.00000000

**Table 4.** Validation of LLM results for velocity when:  $\beta_1 = \beta_2 = M = \theta_f = 1, \phi = 0.01, Ra = 0.5, \gamma = 1, Pr = 6.8, Ec = 0.1, G = 1, R = 1, m = 3$ .

$y$	$u_{LLM}(y)$	$u_{RK4}(y)$	$ u_{LLM} - u_{RK4} $
0.0	0.0000000000000000	0.0000000000000000	0.0000000000
0.2	0.04031441474884955	0.04031441475827205	$9.42250 \times 10^{-12}$
0.4	0.06222933909835976	0.06222933912645120	$2.80914 \times 10^{-11}$
0.6	0.06414832639662879	0.06414832648711902	$9.04902 \times 10^{-11}$
0.8	0.04408622150954411	0.04408622182947682	$3.19933 \times 10^{-10}$
1.0	0.0000000000000000	$3.6244 \times 10^{-12}$	0.0000000000

**Table 5.** Validation of LLM results for temperature when:  $\beta_1 = 1, \beta_2 = 1, \theta_f = 1, \phi = 0.01, M = 1, Ra = 0.5, \gamma = 1, Pr = 6.8, Ec = 0.1, G = 1, R = 1, m = 3$ .

$y$	$\theta_{LLM}(y)$	$\theta_{RK4}(y)$	$ \theta_{LLM} - \theta_{RK4} $
0.0	0.9125189148462466	0.9125189148472346	$9.87987 \times 10^{-13}$
0.2	0.8921648635663214	0.8921648318426922	$3.17236 \times 10^{-8}$
0.4	0.8632813168173238	0.8632812232251493	$9.35922 \times 10^{-8}$
0.6	0.8216871044428341	0.8216869210586025	$1.83384 \times 10^{-7}$
0.8	0.7595470252170218	0.7595465966603754	$4.28557 \times 10^{-7}$
1.0	0.6602479343870364	0.6602479343038165	$8.32200 \times 10^{-11}$

### 4. Discussion of Results

This section investigates the impressions of several significant features that include the variability factor ( $\gamma$ ), nanoparticle volume fraction ( $\phi$ ), magnetic factor ( $M$ ), Reynold’s number ( $R$ ), Radiation factor ( $Rd$ ), Biot numbers number ( $\beta_1, \beta_2$ ), Eckert number ( $Ec$ ), against the velocity  $u(y)$ , temperature  $\theta(y)$ , skin friction  $C_f$  and Nusselt number ( $Nu$ ). The nanoparticle volume fraction is defined as  $\phi$  falling between 0% and 6%, with 0 denoting pure base fluid. Additionally, the radiation parameter is allocated a range of  $0.1 \leq Rd \leq 0.7$ , the Reynolds number  $1 \leq R \leq 4$ , and the thermal conductivity variation parameter is assigned a range of  $0.1 \leq \gamma \leq 1.0$ , the Brinkman number  $0.1 \leq Ec \leq 0.7$ , and the magnetic parameter  $0 \leq M \leq 5$ . The dimensionless pressure gradient is kept fixed at  $G = 1$ . The impact of the variability parameter ( $\gamma$ ) on the Cu–water nanofluid velocity and temperature profiles, as seen in Figures 3 and 4, is a significant factor in laminar flow. In Figure 3, when the variability parameter ( $\gamma$ ) increases, the Cu–water nanofluid velocity dramatically increases and the temperature drops. With higher values of the variability parameter ( $\gamma$ ), the flow distribution becomes more parabolic, with the highest value near the channel’s centerline and the minimum at the walls. The fluid gets more flow-resistive as the parameter values rise, enhancing the flow motion. This means that in order to overcome the increased resistance, the flow must accelerate more quickly. Additionally, the increased convective heat transfer may be responsible for the drop in the Cu–water nanofluid thermal profile.

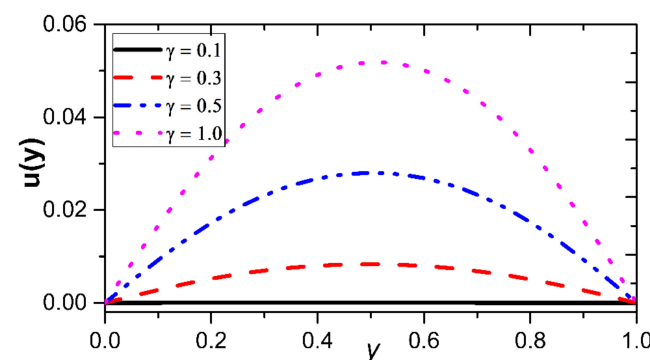


**Figure 3.** Effect of  $\gamma$  on the velocity.

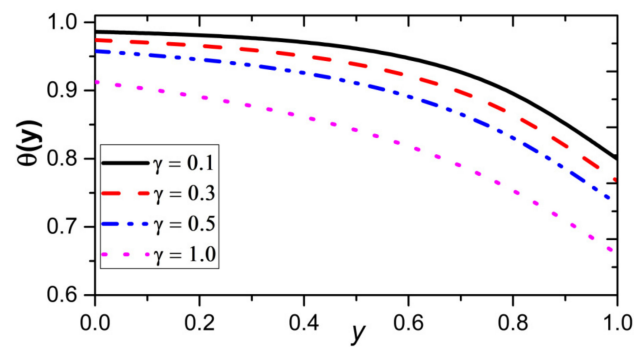


Figure 4. Effect of  $\gamma$  on the temperature.

Figures 5 and 6 depict the consequences of the magnetic parameter ( $M$ ) on the Cu–water nanofluid velocity and temperature profiles. In magnetohydrodynamic (MHD) flow, the Lorentz force interaction with the flow alters the Cu–water nanofluid velocity profile. This force tends to oppose the flow motion, resulting in Cu–water nanofluid velocity reduction. Similarly, in Figure 6, the temperature profile is influenced by the enhanced magnetic parameter ( $M$ ) through a magnetohydrodynamic (MHD) cooling phenomenon. The fluctuation in the Cu–water nanofluid velocity and temperature profiles temperature profile is depicted in Figures 7 and 8, respectively, for values varying numbers of volume fraction factor ( $\phi$ ). It has been reported with clarity that by raising the volume fraction factor ( $\phi$ ), the copper particles form clusters due to attractive force between them. These clusters act as an obstruction to the flow, thereby impeding flow motion, which results in a drop in the velocity profile. Furthermore, as elucidated in Figure 8, with the introduction of copper particles into the base liquid, the effective thermal conductivity of the mixture is thereby enhanced. This promotes more efficient heat transfer giving rise to heat dissipation and leading to a decrease the thermal distribution.

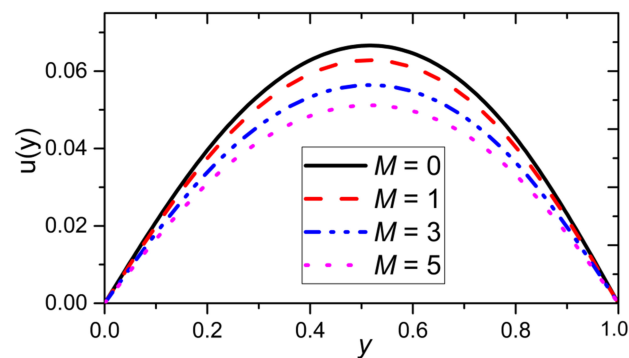


Figure 5. Effect of  $M$  on the velocity.

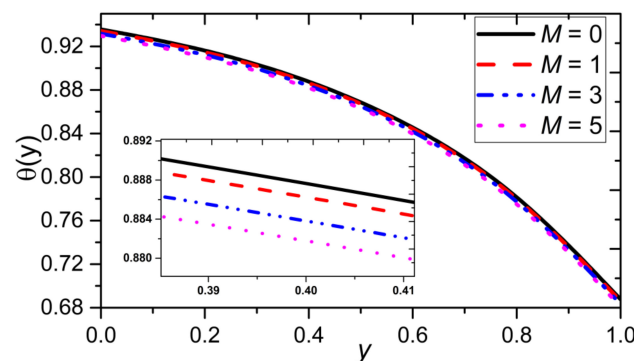


Figure 6. Effect of  $M$  on the temperature.

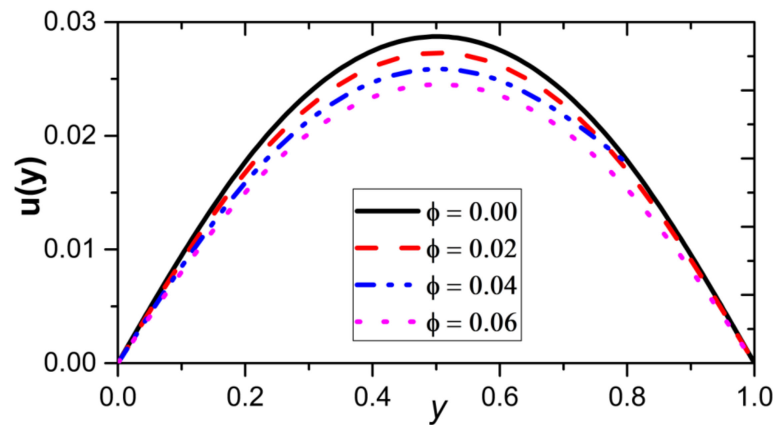


Figure 7. Effect of  $\phi$  on the velocity.

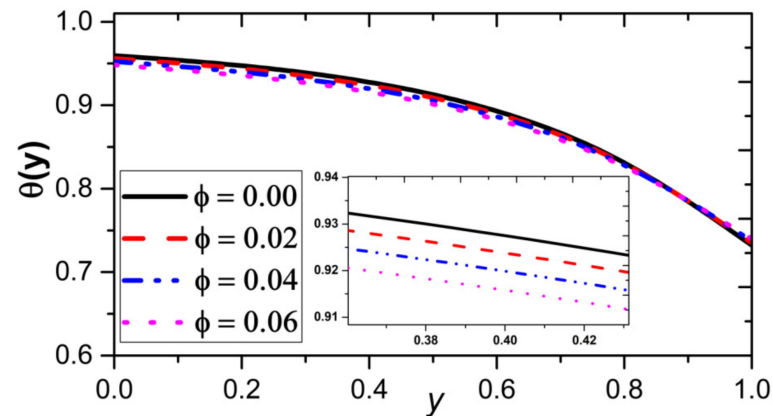


Figure 8. Effect of  $\phi$  on the temperature.

Figures 9 and 10 indicate the effect of Reynolds number ( $R$ ) on the Cu–water nanofluid velocity and temperature profiles, respectively. The Cu–water nanofluid velocity decreases near the lower fixed wall and increases near the upper fixed wall due to an increase in the values of Reynolds number ( $R$ ). The physics behind such fluctuations is that as the Reynolds number becomes larger, the flow becomes more prone to turbulence. This turbulence effect translates to enhance mixing and increases the momentum transfer, which could result in a boost in the flow motion. Furthermore, the enhanced mixing could also lead to improvement in the convective heat transfer, increasing temperature gradient. As seen in Figure 11, an increment in the radiation factor ( $R_d$ ) results in a decline in the Cu–water nanofluid velocity. This is expected as the fluid viscosity is reduced due to higher temperature impacting the velocity profile by reducing the resistance to flow, consequently decreasing the nanofluid velocity. On the other hand, as illustrated in Figure 12, the Cu–water nanofluid temperature profile decreases as the radiation factor ( $R_d$ ) increases. This effect is a result of increasing convective heat transfer counterbalancing the impact of thermal radiation, which results in a Cu–water nanofluid temperature decrease. The consequences of the upper and lower Biot numbers ( $\beta_1$  and  $\beta_2$ ) on the Cu–water nanofluid temperature profiles are displayed in Figures 13 and 14, respectively. It is observed that the enhancing the values of the upper Biot number, the thermal distribution declines as well. Physically, the convective Biot number represents the ratio of thermal resistance within the solid to the thermal resistance at the fluid–solid interface. By increasing the convective heat transfer coefficient, the rate of convective heat transfer will thereby increase, which consequently results in a more pronounced reduction in the Cu–water nanofluid temperature profile. Conversely, higher thermal conductivity, which is a sign of efficient

heat conduct, leads to a reduction in the temperature gradient and enhances the temperature profile. In Figure 15, enhanced values of Eckert number ( $Ec$ ) slightly decrease the Cu–water nanofluid temperature profile. For a larger Eckert number, the increased kinetic energy can lead to larger dissipation of mechanical energy into thermal energy via a viscous effect. This intensifies dissipation, thereby resulting in a slight Cu–water temperature increase.

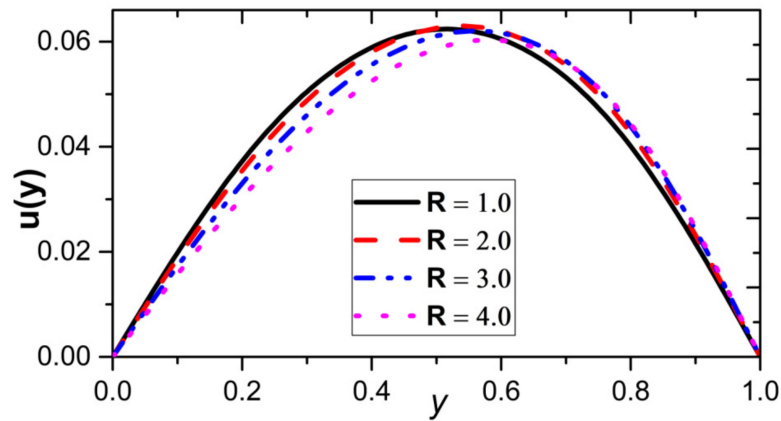


Figure 9. Effect of  $R$  on the velocity.

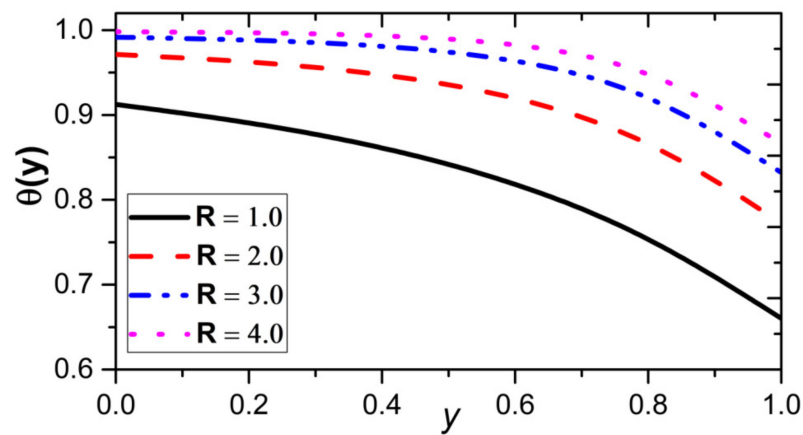


Figure 10. Effect of  $R$  on the temperature.

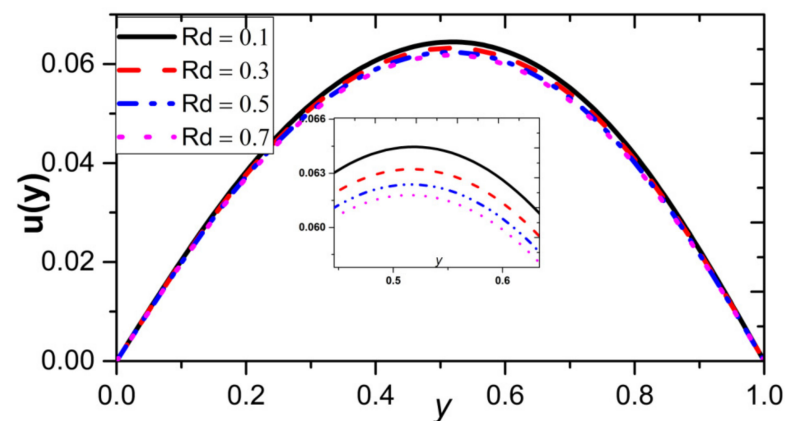


Figure 11. Effect of  $Rd$  on the velocity.

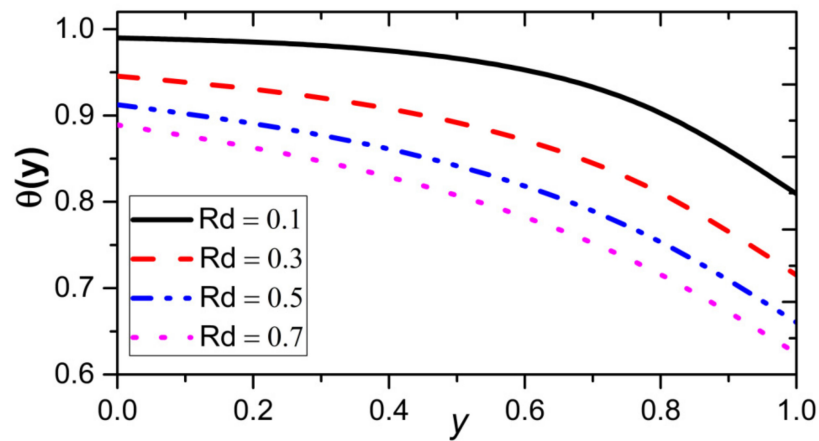


Figure 12. Effect of  $Rd$  on the temperature.

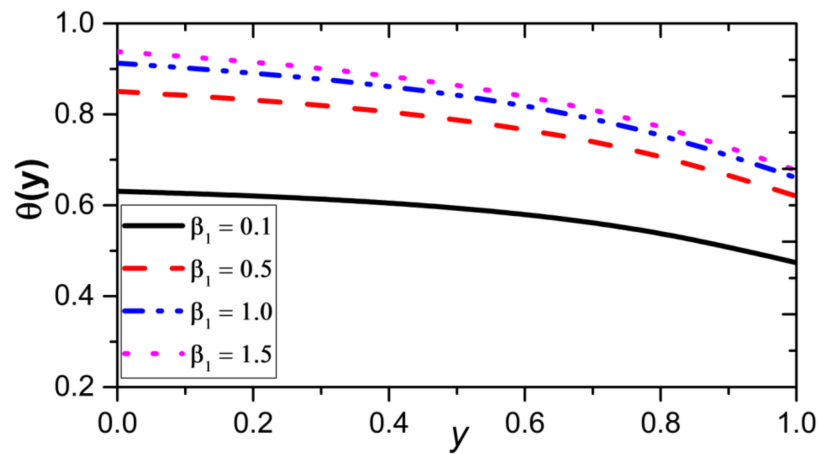


Figure 13. Effect of  $\beta_1$  on the temperature.

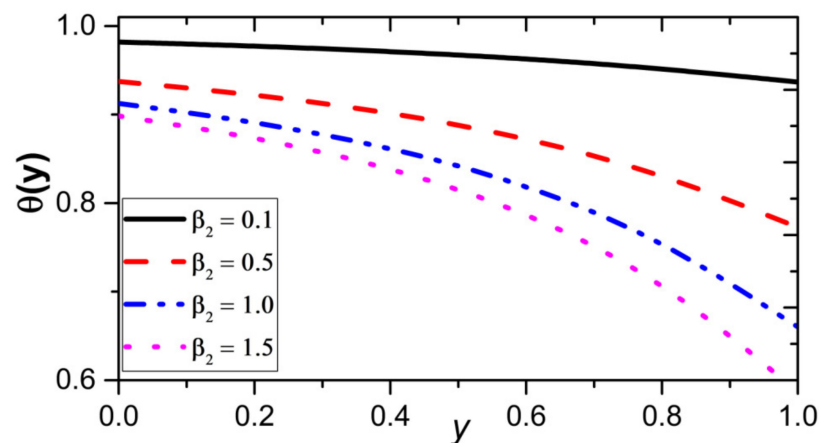


Figure 14. Effect of  $\beta_2$  on the temperature.

Figures 16–18 depict how several factors affect skin friction. With increasing the upper and lower Biot numbers ( $\beta_1$  and  $\beta_2$ ), Eckert number ( $Ec$ ), variability parameter ( $\gamma$ ), volume fraction parameter ( $\phi$ ), and heat radiation absorption ( $Rd$ ), a reduction in the skin friction coefficient becomes apparent at the inner surface of the channel. As the value of these parameters rises, the fall in skin friction may be linked to a decline in the velocity gradient at the interior of the channel. Moreover, in Figures 19–21, the tendency appears to reverse, with a rise in the rate of channel surface heat transfer as measured by the upper and lower

Biot numbers ( $\beta_1$  and  $\beta_2$ ), the Eckert number ( $Ec$ ), the variability parameter ( $\gamma$ ), the volume fraction parameter ( $\phi$ ), and the absorption of thermal radiation ( $Rd$ ). As such variables grow, the rise in the temperature disparity at the boundary of the channel may be the cause of the rising Nusselt number. The increase in the Nusselt number may be attributed to a rise in the temperature gradient at the channel surface as these parameters increase.

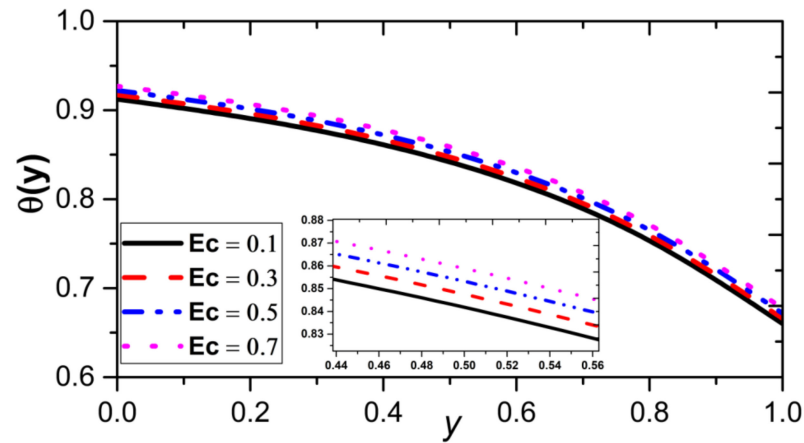


Figure 15. Effect of  $Ec$  on the temperature.

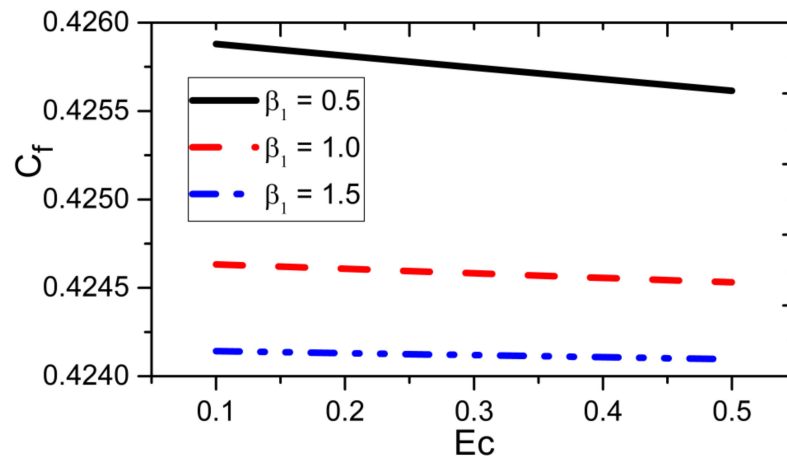


Figure 16. Effect of  $Ec$  and  $\beta_1$  on the skin friction coefficient.

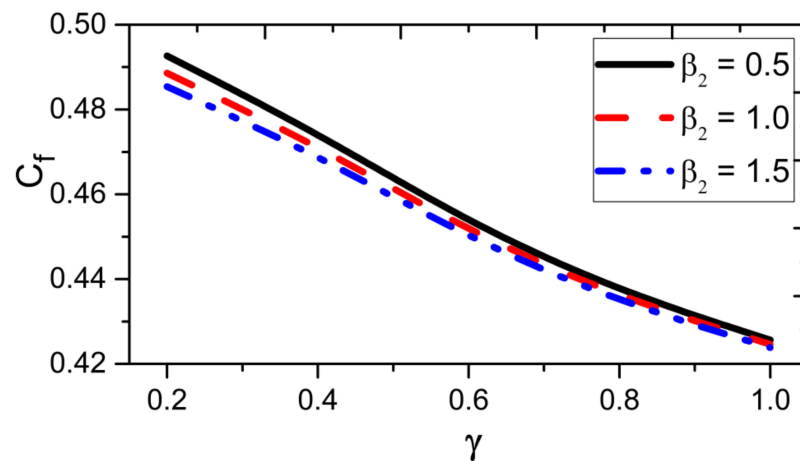


Figure 17. Effect of  $\gamma$  and  $\beta_2$  on the skin friction coefficient.

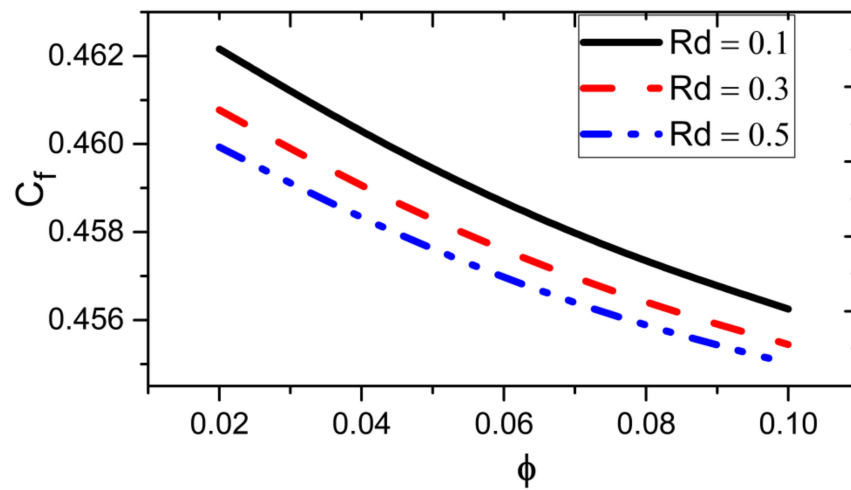


Figure 18. Effect of  $\phi$  and  $Rd$  on the skin friction coefficient.

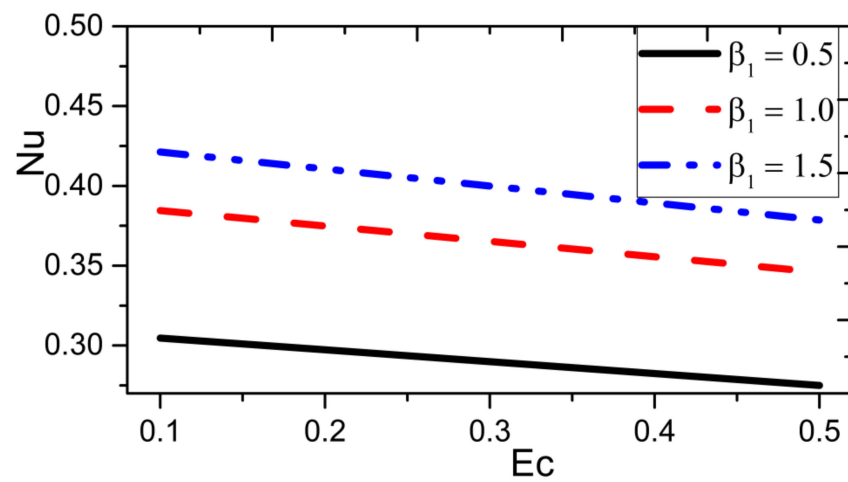


Figure 19. Effect of  $Ec$  and  $\beta_1$  on the Nusselt number.

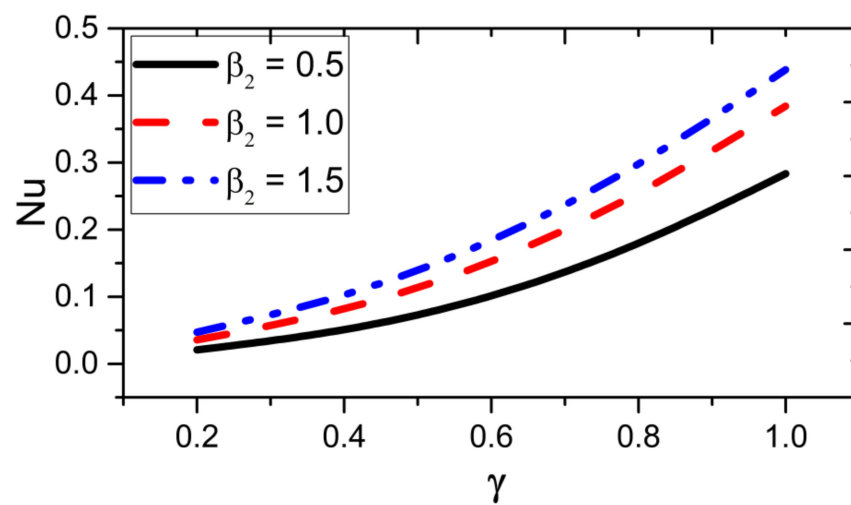


Figure 20. Effect of  $\gamma$  and  $\beta_2$  on the Nusselt number.

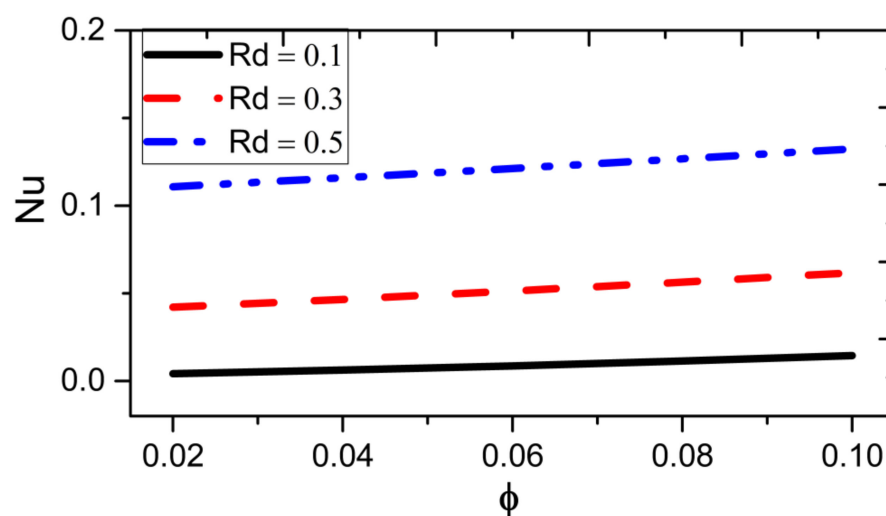


Figure 21. Effect of  $\phi$  and  $Rd$  on the Nusselt number.

## 5. Conclusions

Considering the influence of the temperature-dependent nanofluid viscosity, which is expressed in the Arrhenius model, the momentum and heat balance behaviour of magnetohydrodynamic copper–water nano liquids through a permeable channel are examined in this study. Additionally, viscous dissipation and Ohmic heating are taken into consideration, and the nonlinear thermal radiation heat flow model is used to describe the heat transfer. Finally, the Spectral Local Linearization Method (SLLM) is used to solve the generated governing nonlinear model. The outcomes of the current analysis are as follows:

- The Cu–water nanofluid velocity profile rises with increasing values of the viscosity variable parameter.
- The water/Cu nanofluid temperature field exhibits a rising Reynold’s number behaviour while degrading the value of  $Rd$ .
- The viscosity variable parameter and the volume fraction term of the Cu particles both have a lowering effect on the heat distribution of the water/Cu nanofluid.
- Skin friction coefficients are lowered in magnitude with higher values of heat radiation and volume fraction parameter.
- The rate at which heat travels increases at the channel surface as values of  $\gamma$  and  $\beta_2$  are increased.

The current research has been investigated to determine the increase in thermal efficiency when utilizing water/Cu nanofluid owing to the viscosity variations and nonlinear thermal radiation through examining the combined impacts of nonlinear thermal radiation and nanofluid channel flow. In addition, it advances the understanding of the heat transfer processes that take place in these systems and investigates the technical sectors in which they may be used.

**Author Contributions:** Conceptualization, T.A.Y.; methodology, T.A.Y. and A.T.A.; software, A.T.A. and V.O.A.; validation, O.J.A.; formal analysis, V.O.A.; investigation, A.T.A. and O.J.A.; resources, R.S.L.; writing—original draft, T.A.Y.; writing—review & editing, V.O.A.; supervision, R.S.L.; project administration, O.J.A.; funding acquisition, R.S.L. All authors have read and agreed to the published version of the manuscript.

**Funding:** This research received no external funding.

**Data Availability Statement:** Not applicable.

**Conflicts of Interest:** The authors declare no conflict of interest.

## References

1. Rehena, N.; Alim, M.A. Entropy generation by nanofluid with variable thermal conductivity and viscosity in a flat plate solar collector. *Int. J. Eng. Sci. Technol.* **2015**, *7*, 80–93.
2. Giwa, S.O.; Adegoke, K.A.; Sharifpur, M.; Meyer, J.P. Research trends in nanofluid and its applications: A bibliometric analysis. *J. Nanoparticle Res.* **2022**, *24*, 63. [[CrossRef](#)]
3. Younes, H.; Mao, M.; Murshed, S.S.; Lou, D.; Hong, H.; Peterson, G.P. Nanofluids: Key Parameters to Enhance Thermal Conductivity and its Applications. *Appl. Therm. Eng.* **2022**, *207*, 118202. [[CrossRef](#)]
4. Gürdal, M.; Arslan, K.; Gedik, E.; Minea, A.A. Effects of using nanofluid, applying a magnetic field, and placing turbulators in channels on the convective heat transfer: A comprehensive review. *Renew. Sustain. Energy Rev.* **2022**, *162*, 112453. [[CrossRef](#)]
5. Hussain, S.M.; Jamshed, W.; Safdar, R.; Shahzad, F.; Nasir, N.A.A.M.; Ullah, I. Chemical reaction and thermal characteristics of Maxwell nanofluid flow-through solar collector as a potential solar energy cooling application: A modified Buongiorno's model. *Energy Environ.* **2022**. [[CrossRef](#)]
6. Wang, J.; Xu, Y.P.; Qahiti, R.; Jafaryar, M.; Alazwari, M.A.; Abu-Hamdeh, N.H.; Selim, M.M. Simulation of hybrid nanofluid flow within microchannel heat sinks considering porous media analyzing CPU stability. *J. Petrol. Sci. Eng.* **2022**, *208*, 109734. [[CrossRef](#)]
7. Narayana, P.V.S.; Venkateswarlu, B.; Venkataramana, S. Thermal radiation and heat source effects on an MHD nanofluid past a vertical plate in a rotating system with a porous medium. *Heat Tran. Asian Res.* **2015**, *44*, 1–19. [[CrossRef](#)]
8. Izadi, M.; Sheremet, M.A.; Mehryan, S.A.M.; Pop, I.; Oztop, H.F.; Abu-Hamdeh, N. MHD thermogravitational convection and thermal radiation of a micropolar nanofluid in a porous chamber. *Int. Commun. Heat Mass Tran.* **2020**, *110*, 104409. [[CrossRef](#)]
9. Monaledi, R.L. Inherent irreversibility in Cu–H<sub>2</sub>O nanofluid Couette flow with variable viscosity and nonlinear radiative heat transfer. *Int. J. Fluid Mech. Res.* **2019**, *46*, 525–543. [[CrossRef](#)]
10. Bhandari, A. Water-based Fe<sub>3</sub>O<sub>4</sub> ferrofluid flow between two rotating disks with variable viscosity and variable thermal conductivity. *Int. J. Appl. Comput. Math.* **2021**, *7*, 46. [[CrossRef](#)]
11. Adesanya, S.O.; Yusuf, T.A.; Lebelo, R.S. Numerical investigation on the magnetized reactive viscous couple stress fluid flow down an inclined Riga plate with variable viscosity. *Mathematics* **2022**, *10*, 4713. [[CrossRef](#)]
12. Kumar, K.G.; Chamkha, A.J. Darcy-Forchheimer flow and heat transfer of water-based Cu nanoparticles in convergent/divergent channel subjected to particle shape effect. *Eur. Phys. J. Plus* **2019**, *134*, 107. [[CrossRef](#)]
13. Khan, S.U.; Ali, N.; Mushtaq, T.; Rauf, A.; Shehzad, S.A. Numerical computations on flow and heat transfer of casson fluid over an oscillatory stretching surface with thermal radiation. *Therm. Sci.* **2019**, *23*, 3365–3377.
14. Al-Mdallal, Q.M.; Renuka, A.; Muthamilselvan, M.; Abdalla, B. Ree-Eyring fluid flow of Cu-water nanofluid between infinite spinning disks with an effect of thermal radiation. *Ain Shams Eng. J.* **2021**, *12*, 2947–2956. [[CrossRef](#)]
15. Khan, M.; Ahmed, J.; Rasheed, Z. Entropy generation analysis for axisymmetric flow of Carreau nanofluid over a radially stretching disk. *Appl. Nanosci.* **2020**, *10*, 5291–5303. [[CrossRef](#)]
16. Rooman, M.; Jan, M.A.; Shah, Z.; Vrinceanu Bou, F.S.; Iqbal, S.; Deebani, W. Entropy Optimization on Axisymmetric Darcy–Forchheimer Powell–Eyring Nanofluid over a Horizontally Stretching Cylinder with Viscous Dissipation Effect. *Coatings* **2022**, *12*, 749. [[CrossRef](#)]
17. Bellman, R.E.; Kalaba, R.E. *Quasilinearisation and Non-Linear Boundary-Value Problems*; Elsevier: Amsterdam, The Netherlands, 1965.
18. Motsa, S.S.; Dlamini, P.G.; Khumalo, M. Spectral relaxation method and spectral quasilinearization method for solving unsteady boundary layer flow problems. *Adv. Math. Phys.* **2014**, *2014*, 341964. [[CrossRef](#)]
19. Yusuf, T.A. Analysis of entropy generation in nonlinear convection flow of unsteady magneto-nanofluid configured by vertical stretching sheet with Ohmic heating. *Int. J. Ambient Energy* **2023**, *44*, 2319–2335. [[CrossRef](#)]
20. Motsa, S.S.; Makukula, Z.G.; Shateyi, S. Spectral local linearization approach for natural convection boundary layer flow. *Math. Probl. Eng.* **2013**, *2013*, 765013. [[CrossRef](#)]
21. Magagula, V.M.; Motsa, S.S.; Sibanda, P.; Dlamini, P.G. On a bivariate spectral relaxation method for unsteady magneto-hydrodynamic flow in porous media. *SpringerPlus* **2016**, *z5*, 455. [[CrossRef](#)]
22. Ibrahim, W. Spectral Quasilinearization Method for Solution of Convective Heating Condition. *Eng. Trans.* **2020**, *68*, 69–87.
23. Makinde, O.D.; Egunjobi, A.S. Effects of convective heating on entropy generation rate in a channel with permeable walls. *Entropy* **2013**, *15*, 220–223. [[CrossRef](#)]

**Disclaimer/Publisher's Note:** The statements, opinions and data contained in all publications are solely those of the individual author(s) and contributor(s) and not of MDPI and/or the editor(s). MDPI and/or the editor(s) disclaim responsibility for any injury to people or property resulting from any ideas, methods, instructions or products referred to in the content.